High Sensitivity Imaging at Low Radio Frequencies

IISER PUNE

A thesis submitted towards partial fulfilment of

BS-MS Dual Degree Programme

by

Shadab Alam

under the guidance of

Dr. Ramana Athreya

Indian Institute of Science Education and Research

Pune

Certificate

This is to certify that this thesis entitled "High Sensitivity Imaging at Low Radio Frequencies" submitted towards the partial fulfilment of the BS-MS dual degree programme at the Indian Institute of Science Education and Research Pune represents original research carried out by Shadab Alam at INDIAN INSTITUTE OF SCIENCE EDUCATION AND RESEARCH, PUNE, under the supervision of Dr. Ramana Athreya during the academic year 2011-2012.

Student
SHADAB ALAM

Supervisor
RAMANA
ATHREYA

Acknowledgements

Dedicated to Batch 2007 of IISER Pune

Abstract

The Giant Metrewave Radio Telescope (GMRT)[1] currently is the most sensitive low frequency radio telescope in operation. However, there are many problems associated with low frequency radio observations(chap 2). Low frequency radio observation is seriously affect by man-made radio frequency interference and dynamics of the ionosphere. This requires long observation time with high sampling rate in order to obtain good sensitivity. Therefore the data size becomes very large, even as big as 50-200 GB. The huge size of files and recursive way of calibration requires a lot of computing resources. Visual inspection, which is the traditional way of identifying bad data, is totally impractical with these large data sizes.We have implemented a hybrid scheme (Fig.2.7) wherein we carry out most of the analysis on a decimated data set obtained by averaging over several time intervals and channels (section 2.1.1). The key to this scheme is the ability to transfer the results of data processing from the decimated file to the original file(section 2.1.2). With this we save computation time without losing the sensitivity afforded by the full data. We have also implemented algorithm to detect, quantify and correct deviations in residual data if possible else flag them (section 2.1.3). Altogether, we have developed a software tool(Fig.2.7) which handles large data set efficiently and remove many kind of corrupted data by analysing residual UV data file, which improves sensitivity.

We planned to look at two problems which require high sensitivity imaging at low radio frequencies: Feedback from Active Galactic nuclei(AGN)into the cluster medium (section 3.1) and Off-pulse emission of Pulsars(section 3.2).

Contents

Chapter 1

Principles of Interferometry and Imaging

The field of radio astronomy, or the study of astrophysical phenomena in the radio regime of the electromagnetic spectrum, was started by Karl Jansky in 1923. The range of radio wavelength observable from earth extends from 1mm to 30m.

Radio astronomical imaging poses a different set of challenges compared to (traditional) optical astronomy; all of these differences may be traced to the much lower frequency of radio waves, in one way or the other. In particular, the resolution of a telescope (equal to $1.22(\lambda/D)$, where D is the aperture size) is considerably poorer at radio frequencies than in the optical. The scattering in the ionosphere ($\propto \lambda^4$) is much more for radio waves than in the optical. The size of each detector ($\propto \lambda/2$) is also much larger for radio waves. It is not possible to physically construct an array of detectors (charged coupled device for optical) for radio waves.

We need a much bigger radio telescope to achieve the same resolution as an optical telescope, which is impossible to construct due to various limitations. Instead radio astronomers use interferometry (correlated observations using pairs of antennas) to achieve high angular resolution. Each pair of antennas (termed a baseline) measures a particular fourier component (termed

as visibility) of the sky intensity distribution. The fourier transform of a set of visibilities (in the U-V plane) yields the intensity distribution in the sky plane. Martin Ryle received the Nobel prize in physics in 1974 for developing an efficient technique of radio imaging called aperture synthesis using the above principle. Radio astronomers synthesise a large telescope by putting together a large number of widely separated baselines using antennas of much smaller size ... and hence the name *aperture synthesis*[7]. These antennas, connected in pairs, yield a resolution equivalent to a single dish telescope of the size equal to the largest baseline in the set. This makes it possible to achieve high resolution at lower frequency without building a very large antenna. The idea of aperture synthesis is based on the Van Cittert Zernike theorem[8].

1.1 Van Cittert-Zernike Theorem

The Van Cittert-Zernike theorem relates the spatial correlation of the electric fields measured at two antennas with the sky intensity distribution.

$$\langle E(\vec{r}_1)E^*(\vec{r}_2)\rangle = V(u,v,w) = \int \mathcal{I}(l,m)e^{-2\pi\iota[ul+vm+wn]}\frac{dldm}{\sqrt{1-l^2-m^2}} \quad (1.1)$$

$V(u,v,w)$ is the visibility measured for the baseline coordinates (u,v,w) defined by $u = \dfrac{x_2-x_1}{\lambda}$, $v = \dfrac{y_2-y_1}{\lambda}$ and $w = \dfrac{z_2-z_1}{\lambda}$, λ is the wavelength of observation, $\vec{r}_1 \equiv (x_1,y_1,z_1)$ and $\vec{r}_2 \equiv (x_2,y_2,z_2)$ are co-ordinates of the two antenna's of a baseline, $\mathcal{I}(l,m)$ is the intensity distribution of the sky, l,m,n are the direction cosines with respect to the origin in the sky.

There are two situations in which this equation reduces to a regular fourier relationship. When w=0, i.e. the baselines are coplanar, the visibilities becomes the fourier transform of the modified intensity distribution.

$$V(u,v) = \mathcal{F}\left\{\mathcal{I}' = \frac{\mathcal{I}(l,m)}{\sqrt{1-l^2-m^2}}\right\}. \quad (1.2)$$

The second condition is when the source integral covers only a small region of the sky (l and m are very small, and therefore $n \simeq 1$). The use of a large

parabolic antenna naturally meets this requirement.

$$V(u, v, w) = \mathcal{F}\{\mathcal{I}(l, m)\} * e^{-2\pi\iota w}.$$ (1.3)

The above two assumptions, coplanar baselines and imaging of a small region of sky, are not valid at low radio frequency. To take care of the curvature of the sky (W-term effect), one divides the field of view in multiple sections(called facets) and images each one separately under the small-field assumption, thus building up the full field.

1.2   Aperture Synthesis

The image is the fourier transform of visibilities. The U-V baseline vector of an antenna pair corresponds to the projection of the antenna separation perpendicular to the instantaneous direction to the source (see Fig. 1.1). Sources at different declinations, or even the same source at different hour angles will result in different baseline vectors for a fixed pair of antennas. Therefore, the earth's diurnal rotation results in the observation of multiple baselines from the same two antennas. This technique of synthesising a large number of baselines through a small number of antennas using earth rotation is known as earth rotation aperture synthesis. Locating the antennas in a Y-configuration (Fig. 1.2b), as has been done at the Very Large Array (USA) and the Giant Metrewave Radio Telescope (India), results in an efficient coverage of the U-V plane1.2.

Combining the 30 antennas of GMRT results in the synthesis of a telescope with resolution equal to that of a single antenna of 25 km diameter. Nevertheless, as is obvious in Fig. 1.2, the UV-coverage is patchy with large gaps in-between. This is equivalent to multiplying a completely filled UV-plane by a sampling function $S(u, v)$, i.e. $V_{obs} = V_{filled} \times S(u, v)$. The sampling function can be represented by a collection of δ-functions at the measured values of u-v. Therefore, the fourier transform of observed visibilities does not directly give the intensity distribution of the sky.
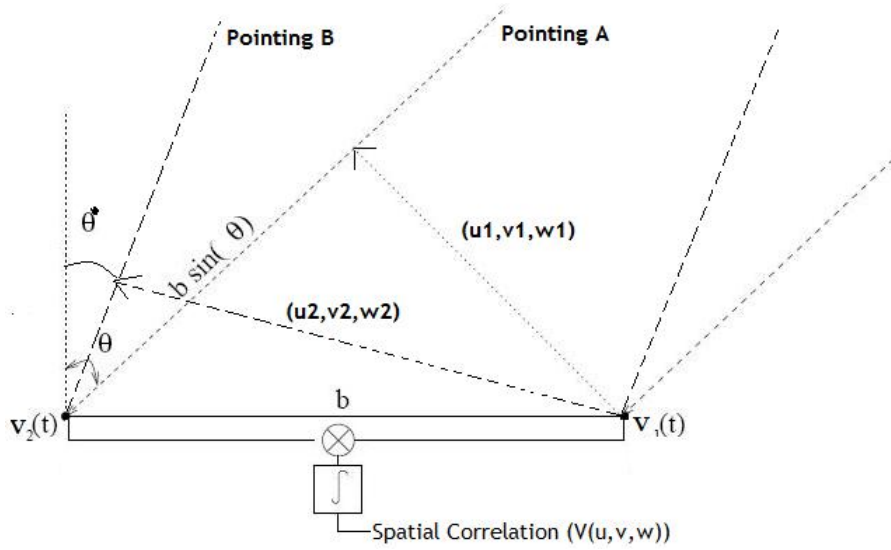
Figure 1.1: A baseline of two element interferometer adapted from [8] The two different pointing (A and B) have different projection of the difference vector, Hence represents different baseline.

$$\mathcal{F}\{V_{obs}\} \; = \; \mathcal{F}\{V(u,v) \times S(u,v)\} = \mathcal{F}\{V(u,v)\} \; \otimes \; \mathcal{F}\{S(u,v)\} \quad (1.4)$$

The fourier transform of the observed visibilities (LHS of eq. (1.4)) is the convolution of the fourier transform of filled visibility with the fourier transform of the sampling function. The fourier transform of the sampling function is termed the *dirty beam* because of its irregular structure. The convolution of the intensity distribution with the dirty beam is called the *dirty map*. Extraction of the sky intensity, called the *clean image*, from the dirty map involves deconvolution and is called *CLEANing* in radio astronomy jargon.
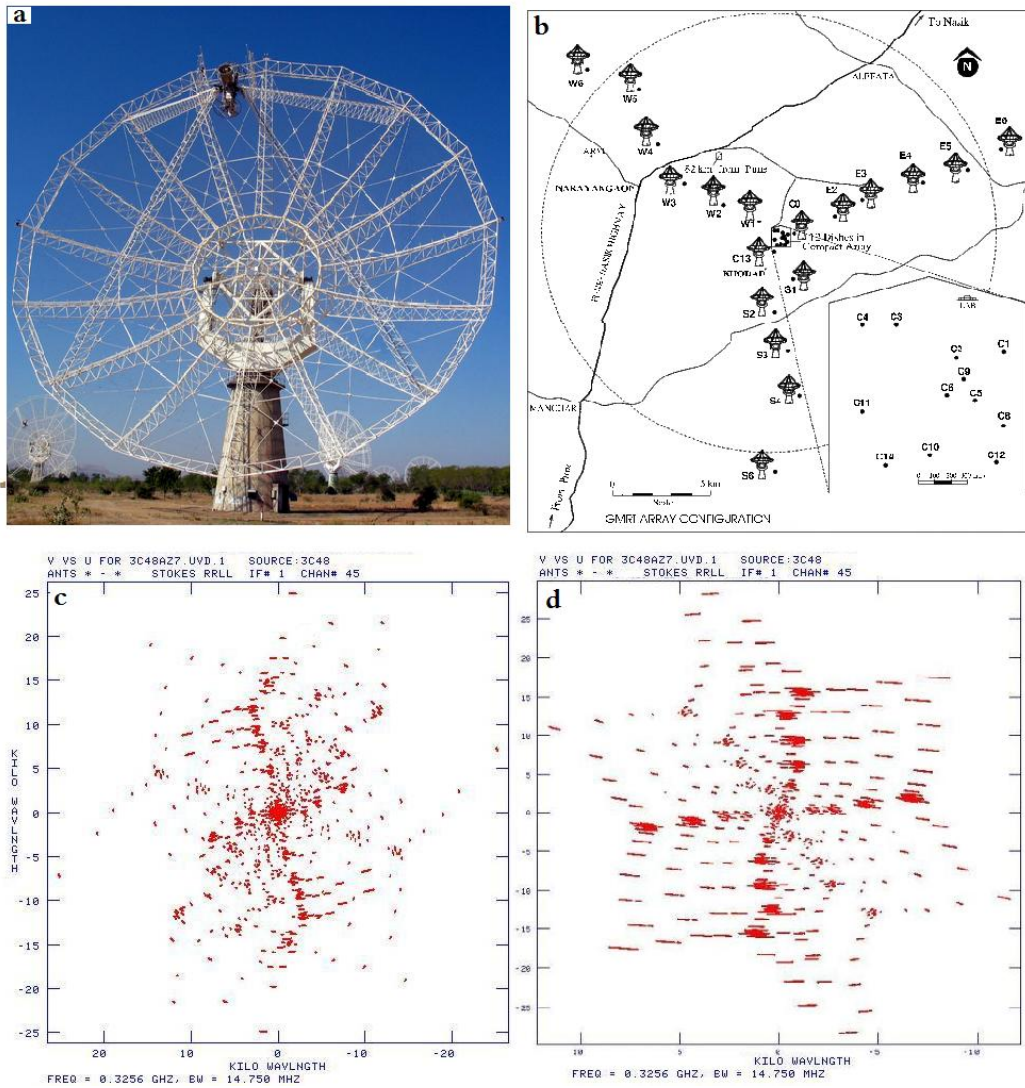
Figure 1.2: **(a)** GMRT 45 metre SMART dish. **(b)** GMRT 30 antenna's configuration with 14 in the central block and rest in 3 Y-shaped arms. **(c,d)** Visibility coverage of the GMRT: The U-V of baseline depends on the antenna configuration and source location. The figure c and d shows UV coverage of GMRT for two different observations. Image courtesy: Basu et al, NCRA Pune

1.3 CLEAN Algorithm

A point source (δ-function) in the sky results in the appearance of a dirty beam pattern in the dirty map.

$$\mathcal{F}\left\{V(u,v)\times S(u,v)\right\} = \delta(\theta,\phi)\otimes\mathcal{F}\left\{S(u,v)\right\} = \mathcal{F}\left\{S(u,v)\right\} \qquad (1.5)$$

The Hogbom CLEAN algorithm [9][10] subtracts discrete dirty beams from a dirty map while adding a corresponding point source in the clean map, until there is no more structure in the residual dirty map. The Hogbom CLEAN works best when the target section of the sky is largely empty and the sources therein are not very extended.

1.4 Calibration

The traverse of a radio wave from the source to the image is affected by various agents which corrupt its amplitude as well as phase; these agents include the ionosphere, receiver electronics, radio frequency interference from human activities, etc. Therefore, the instrument has to be calibrated to convert the measured numbers into a standard unit (e.g. flux density).

$$V_{ij}^{meas}(t) = G_{ij}(t)V_{ij}^{true} + E_{ij}(t) + H_{ij}(t) \qquad (1.6)$$

where V is the visibility (measured and true) for the antenna pair i-j, G is the complex gain, H is the stochastic (gaussian) noise and E represents all the other systematic effects. G_{ij} consists of antenna-based and baseline-based terms:

$$G_{ij}(t) = g_i(t)g_j^*(t) + \delta_{ij} \qquad (1.7)$$

where $g_i(t)$ is the antenna-based complex gain of the ith antenna. The antenna-based gain will be the same for all the baselines of a particular antenna. It can be determined through the technique of self calibration [13][14]. The second term ($\delta_{ij}(t)$) is a baseline-based correction. There is

no standard technique to find baseline correction, which puts a limit on the image sensitivity. In this project we have focused on baseline-based errors, by developing and implementing algorithms to detect and quantify such errors, and correct the data point if possible else flag them.

1.5   Problems and Limitations

1.5.1   Noise and Dynamic range

Thermal noise due to finite system temperature is present in all observations. It is the non-zero rms observed in absence of any source. It is directly proportional to the system temperature and inversely proportional to the root of observation time, number of baseline and bandwidth of observation ($\Delta\nu$).

$$Noise \propto \frac{T_{sys}}{\sqrt{\Delta time \Delta\nu N_{baseline}}} \qquad (1.8)$$

Dynamic range is a measure of the ability to detect the faintest source in presence of a strong source. In radio astronomy dynamic range of an image is defined as the ratio of peak of the strongest source to the minimum rms of noise. It is clearly visible in the Fig.1.3 that noise around a strong source increases with the flux of the source. The figure shows a field around a strong point source 3C286 of flux-density value 27.07 Jy. The plots shows the histogram of pixel intensity inside the boxes A and B. The box A ,near to the strong source, has a large noise 33.9 mJy/Beam. Box B , far away from the strong source, has a smaller noise 14.43 mJy/Beam.

1.5.2   Radio Frequency Interference — RFI

RFI is the main source of corruption at low radio frequencies. They lead to ripples across the image which increase the noise and also corrupt self-cal gain solutions. We are using the software tool RfiX to subtract RFI from data[11]. RfiX identifies and subtracts the oscillating pattern caused by a stationary RFI in the fringed-stopped correlator output of an interferometer
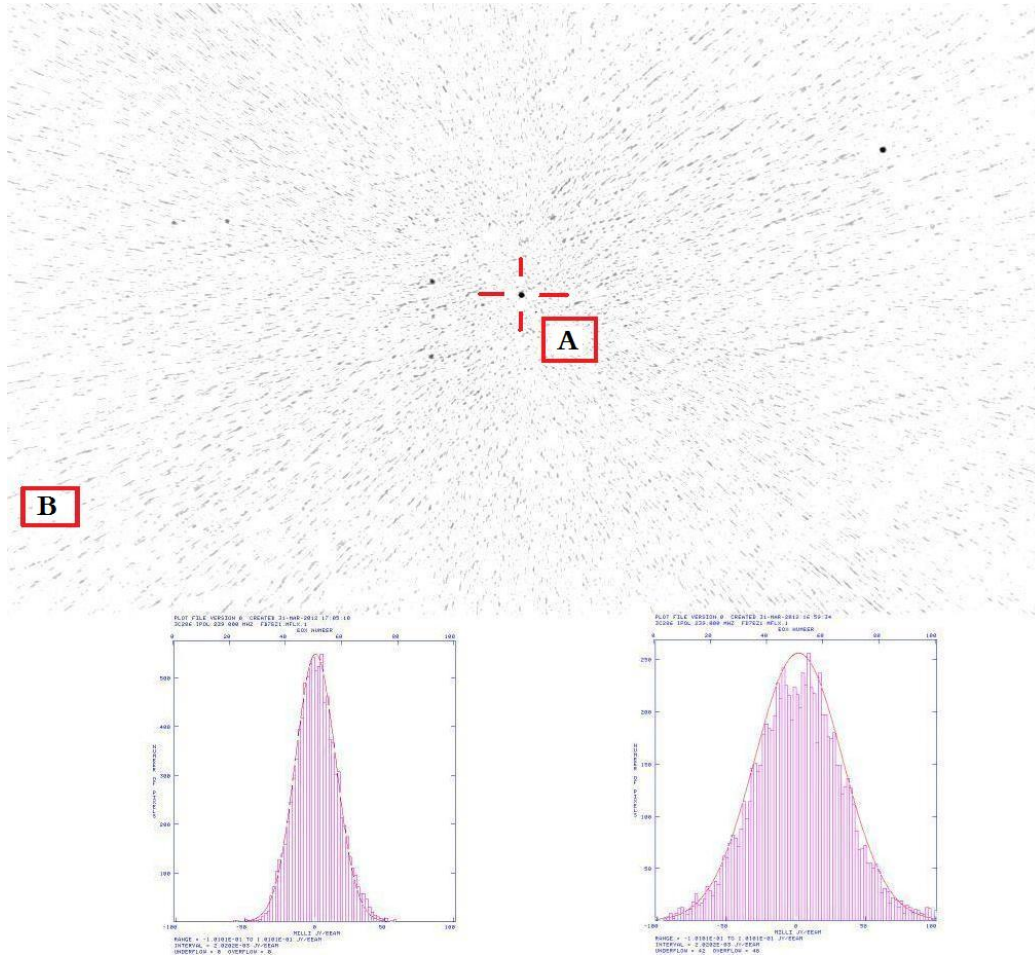
Figure 1.3: **Dynamic Range:** Strong point source 3C286 at the centre (red cross). Left histogram shows the noise far away from the point source (inside box B) with rms 14.43 mJy. Right histogram shows noise near to strong source (inside box A) with rms 33.9 mJy.
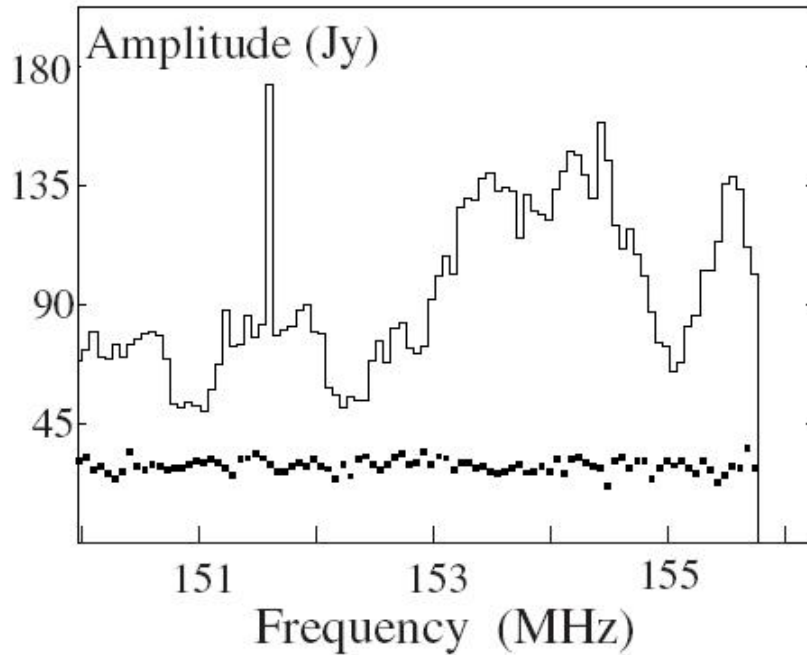
Figure 1.4: **RFI:** Time average amplitude as the function of channel (Band shape). The solid line shows observed data (RFI contaminated) and dotted line shows the true value after processing through RfiX. Image Courtesy: Athreya R [11]

baseline. The Fig. 1.4 shows the data with RFI and True level (processed via RfiX). The RFI changes the band shape and also offset the value of data from its true value. The offset can modify the band level and contribute to the error in the flux.

1.5.3 Correlator offset

The correlator can introduce a constant offset for all times in a baseline. The correlator offset can be due to leakage currents and improper grounding. This offset is very difficult to detect and be present in the data throughout. The correlator offset is different for different baseline and makes high sensitivity imaging more challenging. We don't know much about the nature and effect of the correlator offset.

Chapter 2

Tools for High Sensitivity Imaging at Low Radio Frequencies

The emission from radio sources is characterised by the spectral index α : flux density $S \sim \nu^{\alpha}$. Typically, radio sources have a spectral index of -0.75 while the radio plumes in X-ray cavities, radio halos, relics, and pulsar have spectral indices as steep as -1.5 to -2.0. Therefore, they are most prominent at the lowest radio frequencies (less than 300 MHz). The GMRT [1] is currently the most sensitive low frequency radio telescope in operation. However, there are many problems associated with low frequency radio imaging such as:

1. Low frequency radio bands are seriously affected by man-made radio frequency interference (cell phones, vehicle spark plugs, TV stations, arcing on power lines, industries, etc.) which corrupt the data.

2. The ionosphere behaves as a highly variable screen (both in space and time) introducing phase corruptions and amplitude scintillations in the path of the radio wave, again reducing the image sensitivity.

3. The large fields of view at low radio frequencies mean that one can no longer ignore the curvature of sky (w-term) 1.1 while making an image.
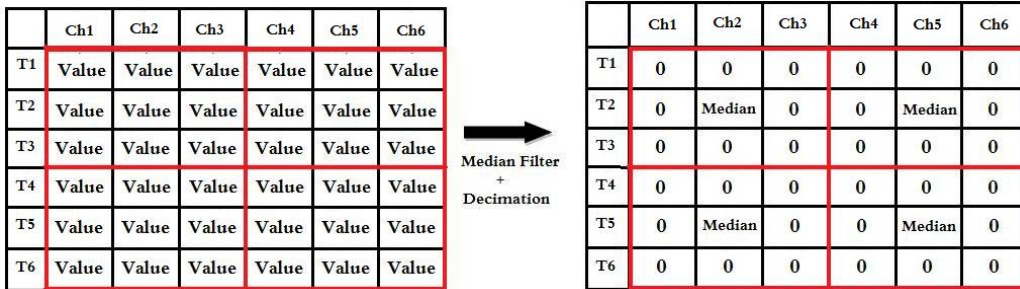
Figure 2.1: Illustration of Median Filter and decimation, The red square shows a 3×3 median block, Four Median blocks are shown in the figure.

This increases the computational requirement by a large amount.

2.1 Reducing Data size

At low radio frequency the corruption rate is high. This requires long observation time with high sampling rate in order to obtain good sensitivity. Therefore the data size becomes very large, even as big as 50-200 GB. The huge size of files and recursive way of calibration requires a lot of computing resources. Visual inspection, which is the traditional way of identifying bad data, is totally impractical with these large data sizes.

2.1.1 Filtering Original Data

We have implemented a hybrid scheme wherein we retain a master data set with the full time and frequency resolution but carry out most of the analysis on a decimated data set obtained by averaging over several time intervals and channels. The key to this scheme is the ability to transfer the results of data processing from the decimated file to the original file. Typically, multiple rounds of self-calibration and data flagging are carried out on the decimated file, after which the same are applied to the original file. With this we save computation time without losing the sensitivity afforded by the full data.

Median Filter

Essentially, data within a grid of m-consecutive time and n-consecutive frequency channels are replaced by one representative value at the centre of the grid, thereby reducing the size of the new data file by a factor $m \times n$. We usually prefer median over mean, because any corruption in the data biases the mean much more than the median.

Two factors determine the largest interval (in time and channel) over which the data may be averaged for decimation. Firstly, we can transfer the calibration and the sky model from the decimated file to the original file without losing information only if interpolation remains within the linear regime. The other constraint comes from the requirement that the averaging scale be smaller than the UV grid size required by the imaging algorithm. Violating this requirement will result in a non-uniform smoothing of visibilities in the U-V plane, and consequently a dirty beam which is variable in time. The standard integration time of 17 seconds of the GMRT appears to be a safe number for our averaging time scale. We typically observe data at 2 second integration time to manage the RFI. Therefore the above scheme will result in the reduction of data size by an factor of ∼8; in the case of pulsars, which are observed at 125 or 250 millisecond interval the reduction could be as high as 125. Averaging over channels reduces the data size by a further factor of 3-7.

2.1.2 Transferring back calibration to the Full file

The ability to transfer back calibration from the decimated file to the full file is essential. The decimated file gets calibrated and imaged several times. The ratio of the final decimated UV file to the initial decimated UV file is used to find the antenna based complex gains. The gains from the decimated file are interpolated across gaps in the data, and also across the decimation grid before being applied to the original file.

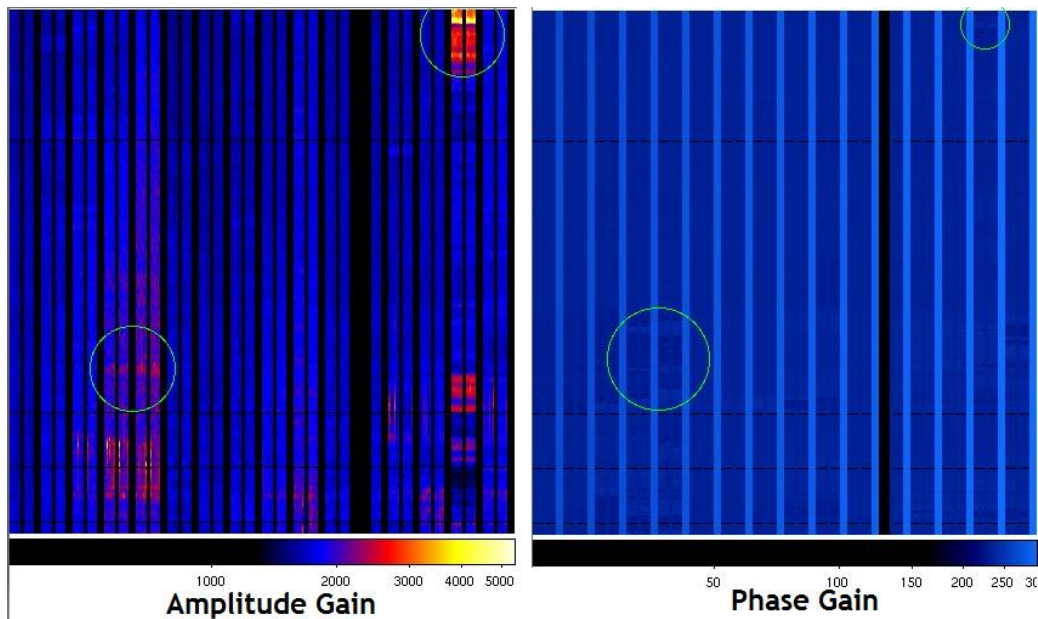Representative gain plots for amplitude and phase are shown in Fig. 2.2.

Figure 2.2: Example of High gain regions

Each stripe in the figure shows the gain for each antenna and polarization. The width of the stripe comes from the channel and the length of the stripe comes from the observation time. Therefore the plot contains gains for all antenna, polarization, channels and times in a compact way. The flagged gains are set to the colour black in the figure. High values of gain may be flagged (see Fig. 2.2) because it usually indicates temporary high variability in the telescope gain or the presence of RFI (due to system saturation). Furthermore, applying high gain corrections usually result in very high rms in the corresponding data regions. Hotspots in the gain may be flagged as required, using a simple threshold scheme.

2.1.3 Model subtraction and Analysis of Residuals

We use the standard software package AIPS (Astronomical Image Processing System) to create a model visibility file for the decimated file. Subtracting the model provides residual visibilities which are easier to analyse for corrupted data. We have a tool for efficiently transferring the sky model from the
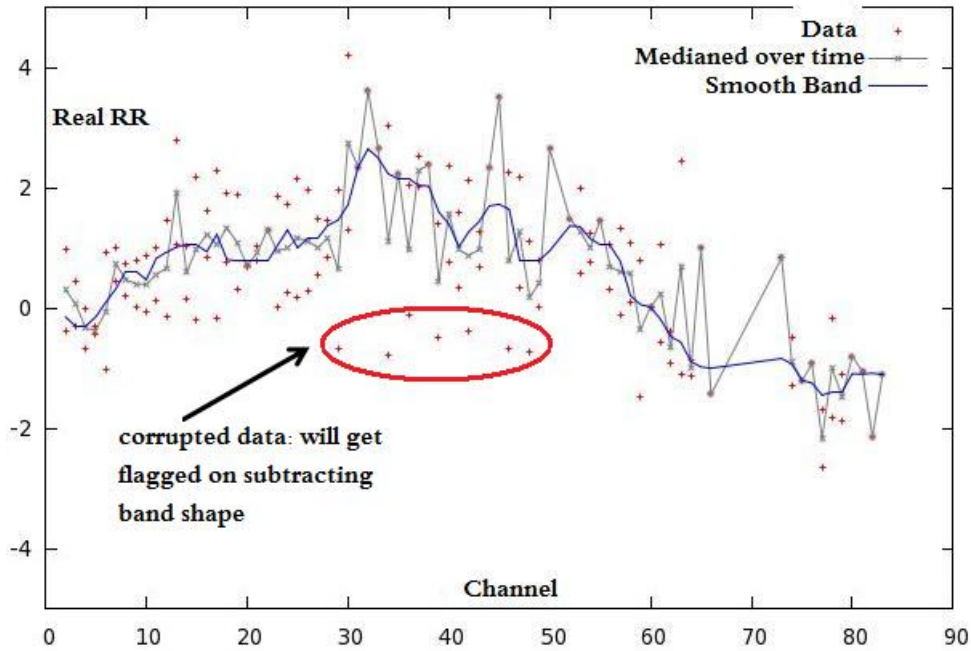
Figure 2.3: **Band Shape:** Band averaged over 20 sec, The red points shows the Real part as the function of channel. Grey line shows the median of Real for each channel over time. On smoothing grey band gives the blue band.

decimated file to the full file. This procedure (of creating the model for the decimated file and then applying it using linear interpolation to the original file) can result in an enormous reduction in processing time.

The most common errors identified in residuals include baseline offsets, distorted band-shapes, non-zero circular polarisation and fluctuating visibilities on very short time scales.

Flatten Band

The band of residual visibilities in Real, Imaginary or Amplitude should be flat or have an rms noise corresponding to the system temperature. We have observed that sometimes data have huge rms or distorted band shapes (Fig. 2.3). While some of the variation is due to the contribution of sources just below the image noise, a substantial fraction of the distortion must

15

be due to the bad data. Our options include flagging data with very bad band-shape, or flattening less corrupted data by subtracting a smoothed pattern. This will only remove the systematic distortions without removing the channel-to-channel noise. Furthermore, the mean for the band is held constant to avoid introducing closure errors. Flattening the band will also help in identifying deviant channels even in the case of bands with legitimate curvature. Of course, in that case the (legitimate) spectral curvature will have to be reapplied to the band after the deviants have been flagged.

Simulations have been used to determine the upper limits of legitimate band curvature due to structure contributed by sources below the noise. Care has been taken to apply the above procedure only for those data which show much higher band distortion than expected from simulations.

Baseline offset

The expected long time average of visibilities (Real/Imaginary) of a baseline is zero. Although the offset value of a single baseline will in general be non-zero the distribution of baseline offsets will be lower than a certain limit depending on the system noise and residual source structure. Any deviation of these baselines from the appropriate value will contribute to increased noise in the image. We have implemented an algorithm to detect, quantify and remove baseline offsets as the function of UV length. Using simulations we studied the contribution of structure due to the source below the noise level in the baseline offset. This provided us with the necessary information to decide upon the various level of flagging and correcting without removing the variation due to source structure. The simulations suggests baseline offset can be divided in three range ($< \Delta_1$, $[\Delta_1, \Delta_2]$, and $> \Delta_2$). Δ_1 is determined from simulations and baselines with offsets less than this value are retained without any modifications. Baselines with deviations above Δ_2 are flagged entirely. The rest of the baselines, with offsets between Δ_1 and Δ_2 may either be shifted to zero offset or a more appropriate value defined by the other polarisation in the data set.
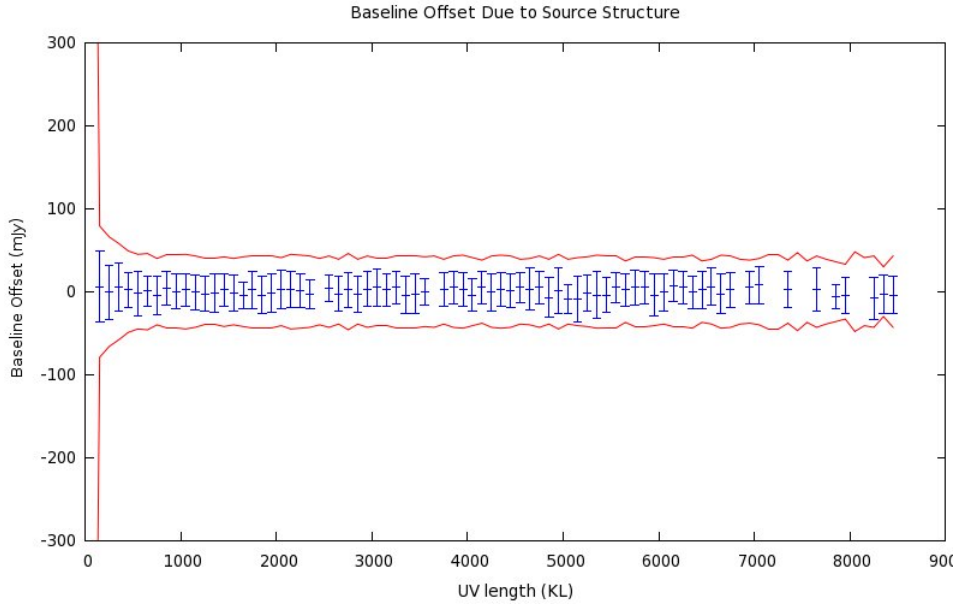
16

Figure 2.4: **Simulate baseline offset:** The plot shows the baseline offset and standard deviation averaged over 8 hours (Blue points) and 2 hours(Red points) of simulation

Figure 2.4 shows the expected distribution of baseline offsets for simulation of a GMRT 150 MHz field with sources above 0.5 mJy truncated to a maximum of 10 mJy (essentially simulating a situation in which the image had been cleaned to a residual of 10 mJy). The red line in the figure shows the standard deviation for the baseline offset averaged over 2 hours of simulation time. The Blue points shows the same averaged over 8 hours of simulation time. Therefore, using a value of Δ_1 outside the envelope plotted in the figure will ensure that legitimate data is not modified.

Circular Polarization Difference

The residuals data should have similar values in both the circular polarizations because we expect Stokes V parameter to be zero in most astrophysical sources. Therefore we have implemented an algorithm to identify data for which the two polarisations are very different and flags the same. Strong
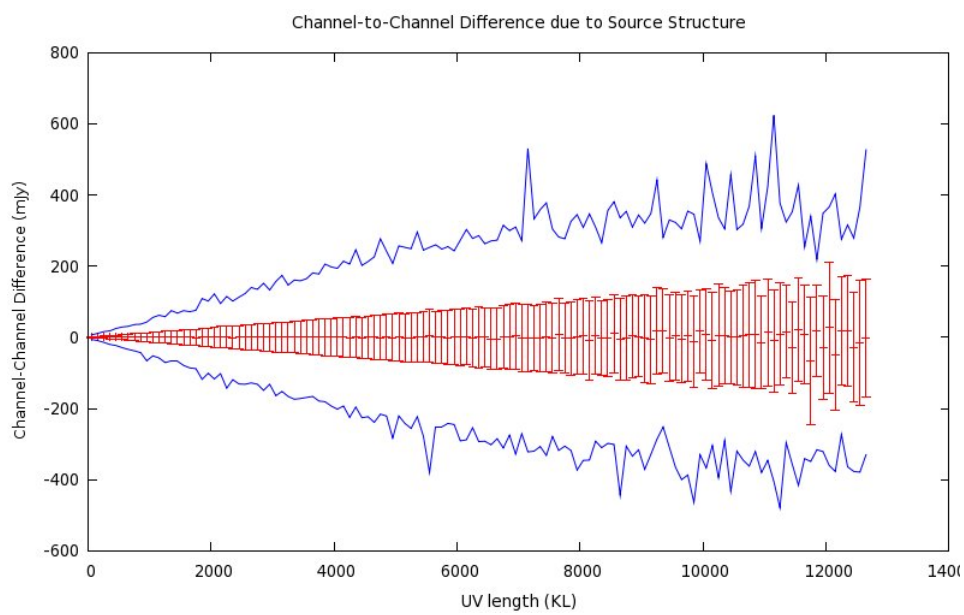
17

Figure 2.5: **Difference in visibility across the band of 62.5 KHz:** The red points shows the mean and standard deviation of baseline offset across the band. The blue curve shows maximum change in visibilities across the band
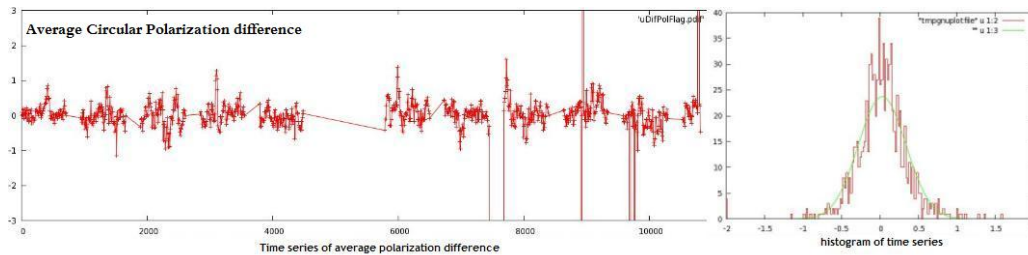
Figure 2.6: **Left Plot:** Time series of difference of amplitude averaged over the channel for the two circular polarization

Right Plot: Histogram of the left plot with a Gaussian fit in green. The extended long tail which needs to be removed is clearly visible in the histogram.

pulsars do show differences in the two circular polarizations and hence this can not be applied to them. But we can apply this flag scheme for faint pulsars because the structure in polarization will be below the noise level for such sources.

The Fig.2.6 shows the plot of difference of amplitude(real/imaginary) for RR and LL circular polarizations averaged over channel as the function of time and its histogram. The large excursions visible in the time series should be corrupted data and will be flagged. The threshold for flagging may also be determined in an automated manner by determining the (gaussian) statistics of the difference between RR and LL polarisations.
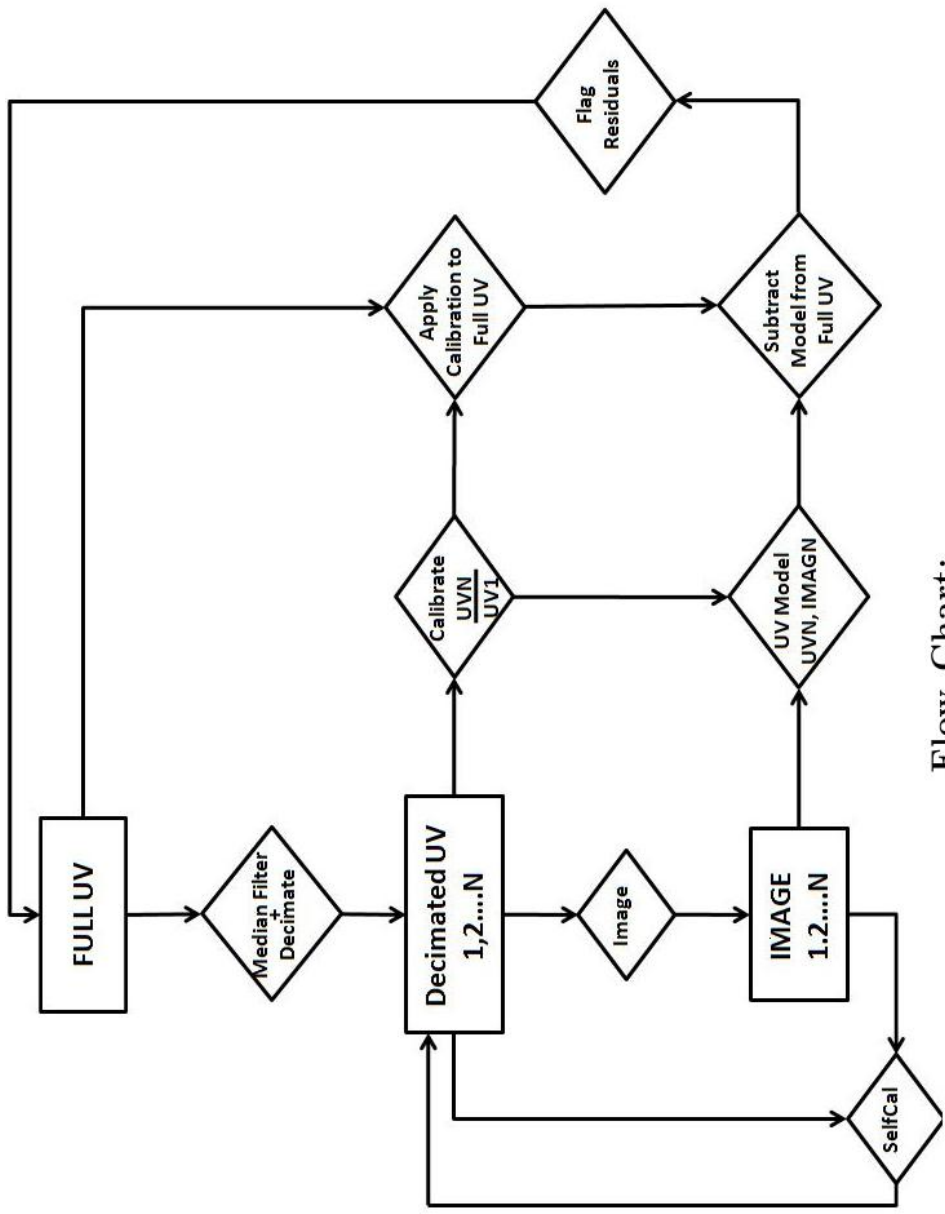
2.2 Simulating Realistic sources

Clearly, good simulations are essential for implementing our schemes to avoid flagging legitimate structure in the residuals. Simulation helped to understand and quantify the effect of sources below the noise level on various quantities like band pass, baseline offset etc. We simulated sources without any noise. We generated realistic source lists during the simulation using published logN-logS data from very deep observations at 1.4 GHz using the

19

VLA and Westerbork. We used realistic UV distributions from real GMRT observations to simulate UV data sets for analysis.

2.3 The Hybrid Scheme

Fig. 2.7 shows the full algorithm for decimation and calibration developed during this project. This is applied after RFI excision using RfiX. We start with a Full UV data file, apply median filter and decimate it to reduce the size, get a decimated UV data file which can be a factor of 5 - 125 smaller than the original file. The decimated UV data file goes through multiple rounds of self-calibration and imaging. The antenna based calibration is calculated using first and last decimated UV data file and then applied to the full data. Similarly the model created for decimated UV data can be applied to the original file. The residual file thus obtained is then analysed and flagged using various flagging schemes described here (median clip, flatten band, baseline offset, Circular Polarization). These flags are transferred to the full UV data file completing one loop of the entire process resulting in a calibrated and flagged original file. The entire loop may be repeated until the best sensitivity is achieved.

Figure 2.7: **Flow Chart:**

Chapter 3

The Astrophysical Problems

We planned to look at two problems which require high sensitivity imaging at low radio frequencies: Feedback from Active Galactic nuclei(AGN)into the cluster medium and Off-pulse emission of Pulsars.

3.1 Active Galactic Nuclei (AGN)

An Active Galactic Nucleus is a compact region at the centre of a galaxy which outputs large amounts of non-stellar luminosity from a galaxy, either in the form of extended radio emission or optical to X-ray emission from an accretion disk. The relativistic jets of an AGN which power the extended radio emission may also transport a significant amount of energy into the surrounding medium (e.g. the intracluster medium(ICM) if the AGN is in a galaxy cluster), through PdV work. This might significantly alter the dynamics of the ICM, e.g. by inhibiting the cooling and in-fall of matter into the centre of the cluster's gravitational potential. In fact, such a process may even affect the AGN since they are believed to be powered by accretion of matter from the ICM into the blackhole within the AGN. Such a feedback loop is termed the AGN feedback.[2]

The cosmological large scale structure evolution simulation in the universe was an attempt to explain the evolution of different structure in the universe

on the basis of existing theories[3]. It predicts that the largest galaxies at the centre of the deep galaxy cluster (gravitational) potential should continuously accrete matter from the surrounding medium. Therefore they should show active star formation and so are expected to be blue in colour. However, observations shows that such galaxies are mostly red in colour with very little active star formation. It has been proposed that the radio AGN sitting near to the centre of the galaxy cluster heats the ICM which slows down, or even stops, the in-fall of matter and suppresses star formation.

Examples of AGN feedback have been observed in the X-ray in the form of ghost cavities (see Fig. 3.1)and the lack of cooling. Chandra and XMM-Newton have shown that the ICM rarely cools below about one third of its original temperature (cooling flow problem) [4] [5]. Further, X-ray images of galaxy clusters with radio AGN show cavities in the smooth background of X-rays. These cavities are known as ghost cavities because in the initial days one did not know the factors responsible for the same. Subsequent radio observations showed radio emission coincident with the X-ray cavities; higher sensitivity radio observations showed that these ghost cavities lie along the expansion of the radio lobes. It has been proposed that the synchrotron plasma in the radio lobes displaces X-ray emitting gas; this displacement of thermal gas by magnetised non-thermal plasma is a more general phenomenon seen in several situations.

We need high sensitivity low radio frequency observation to be able to determine quantitative possibility of proposed phenomenon. Since these sources have steep spectrum we need to do low frequency observation to get sufficient flux. The pressure in the radio plasma (pressure inside the cavity) should be balanced by the pressure in the X-ray gas (pressure outside the cavity). According to Myriam et. al. [6], in the HCG 62 cavity system the estimated X-ray pressure of the cavity is one order of magnitude higher than the equipartition pressure of the radio lobe. This suggest that either energy is not determined by the equipartition point or cavity is supported by AGN feedback with some other phenomenon in this particular system. We need
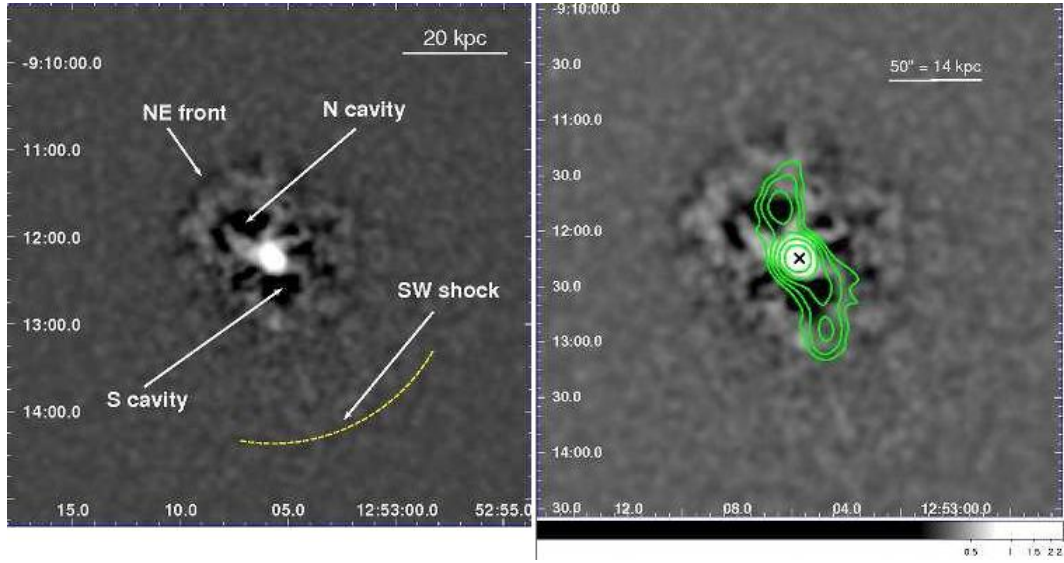
23

Figure 3.1: **Left Image:** Unsharp masked 0.5-2.0 KeV ACIS-S image of the central region of HCG 62.The unsharp masked images are produced by subtracting a large-scale (20 pixels) smoothed image from a small-scale (5 pixels) smoothed image.The dashed arc indicates position of the SW shock. The box is 6060 (101 Kpc by 101 Kpc).North is up and east is left. [6]

Right Image: GMRT 610 MHz contours overlaid on the unsharp masked 0.5-2.0 keV Chandra image. The beam size is 1400 by 1400 . the cross indicates the position of the radio core. The image shows that the radio lobe of the AGN coincide with the cavity in the X-ray image. This show the power of multi wavelength astronomy. North is up and east is left. [6]

to observe many such systems at low frequency and make high sensitivity image to do a statistical analysis to arrive on some results.

3.2 Pulsar off-pulse emission

A pulsar is a compact neutron star which emits intense radiation from the region around the magnetic poles. A misalignment between the rotation and magnetic axes produces pulsed radiation at the observer in the manner of a light house. The pulsar is modelled with dipole magnetic field which has open magnetic field lines at the poles results in the intense emission from the pulsar. There has been several attempts to detect off-pulse emission from the pulsar since its discovery. Recently Basu et. al. [12] detected off-pulse emission from two long period pulsars, PSR B0525+21 and PSR B204516, using the GMRT in interferometric mode. Some of the important reasons for the success were (i) ability to handle very high data rate and volume, (ii) Improved techniques for excising RFI and identifying and flagging bad data and (iii) Observation of the pulsar in the interferometry mode rather than the usual mode of pulsar observations.

The observed data was divided in two parts, comprising the off-pulse and on-pulse regions, and imaged separately. However we now wish to determine the emission in not just two section but in 14 different temporal segments across the pulsar period to determine the off-pulse profile. This higher temporal resolution of the pulse will offer key diagnostics to determine the appropriate theoretical model of off-pulse emission. The proposed higher temporal resolution imaging requires ability to handle huge data volume more efficiently and even higher sensitivity imaging since the data is being divided into smaller temporal segments.

3.3 Results

We have developed all the software tools and understood the various issues associated with data and image quality. We are in the process of applying these tools to observations associated with the above projects.

References

[1] Govind Swarup, Giant Metrewave Radio Telescope(GMRT), ASPC, (1991)

[2] David S. De Young, How Does Radio AGN Feedback Feed Back? arXiv:1001.1178v1 (2010).

[3] Croton, D.J. et al. MNRAS, 365 11-28(2006)

[4] Peterson, et. al.ApJ, 590 207(2003)

[5] Kaastra, et. al. A & A, 413415(2004)

[6] Myriam et. al. arXiv:0912.3013v2 (2010).

[7] http://nobelprize.org/nobel_prizes/physics/laureates/1974/press.html , (1974)

[8] Jayaram N Chengalur, Yashwant Gupta, K. S. Dwarakanath, Low Frequency Radio Astronomy published by NCRA-TIFR.

[9] J. A. Hogbom Astron Astrophys. Suppl. 15 417-426

[10] A. R. Thompson, Interferometry and Synthesis in Radio Astronomy, WILEY- VCH

[11] Athreya R, A New Approach to Mitigation of Radio Frequency Interference in Interferometric data Astrophysical Journal 696:885890 (2009)

[12] Basu et. al., Detection of Off-pulse Emission from PSR B0525+21 and PSR B204516, The Astrophysical Journal, 728:157, (2011)

[13] Tim Cornwell and Edward B Fomalant, Self Calibration, Astronomical Society of Pacific, 185-197, (1989)

[14] Schwab, F. R. , Robust solution for antenna gains, VLA Scientific Memorandum No. 136, NRAO (1980)